Rare Metal Materials and Engineering
Volume 55, Issue 11, November 2026
Available online at www.rmme.ac.cn

Science Press

Cite this article as: Peng Haodong, Li Zhuo, Sun Muqun, et al. Effects of Sr on Microstructure and Properties of Zn-Sn-based Degradable Biomedical Alloys[J]. Rare Metal Materials and Engineering, 2026, 55(11): 2727-2736. DOI: https://doi.org/10.12442/j.issn.1002-185X.20250605.

ARTICLE

Effects of Sr on Microstructure and Properties of Zn-Sn-based Degradable Biomedical Alloys

Peng Haodong[1], Li Zhuo[2,3], Sun Muqun[1], Chen Yingying[2,3], Zhao Linlin[1], Zhang Xin[1]

[1] School of Materials Science and Engineering, Tianjin University of Technology, Tianjin 300384, China; [2] First Teaching Hospital of Tianjin University of Traditional Chinese Medicine, Tianjin 300193, China; [3] National Clinical Research Center for Chinese Medicine, Tianjin 300193, China

Abstract: The microstructure, mechanical properties, corrosion behavior, and cytotoxicity of biodegradable Zn-1.5Sn-*x*Sr alloys (*x*=0, 0.3, 0.5, wt%) were investigated. The results indicate that the addition of Sr introduces minor $SrZn_{13}$ phases, enhancing the yield strength and elastic modulus of the Zn-1.5Sn-*x*Sr alloys. Transmission electron microscopy analysis reveals the existence of the $SrZn_{13}$ phase through the calibration of diffraction spots. Electrochemical tests confirm the formation of a passive film on Zn-1.5Sn-*x*Sr alloys, with Zn-1.5Sn-0.3Sr alloy exhibiting higher corrosion resistance. Further immersion tests and X-ray photoelectron spectroscopy analysis elucidate the elemental composition and content of the passive film formed by the corrosion products, which primarily consists of oxides, hydroxides, and slightly soluble carbonates and phosphates. In terms of cytotoxicity, the Zn-1.5Sn-*x*Sr alloys exhibit excellent biocompatibility. MTT experiments show that the cell viability can reach up to 130%, which is attributed to the release of Sr^{2+} during the degradation. Sr^{2+} and Zn^{2+} ions jointly promote the cell proliferation and differentiation.

Key words: biomedical alloy; degradable alloy; mechanical property; biocompatibility

1 Introduction

Biodegradable metallic materials have garnered significant interest from researchers due to their remarkable biodegradability, biocompatibility, and mechanical compatibility. The most notable feature of these materials is their capacity to degrade naturally within the human body environment. Their degradation products are non-toxic and can be expelled through the metabolic processes of the human body, negating the need for a secondary surgery to remove the implant. This not only simplifies the surgical procedures, but also minimizes the discomfort experienced by patients during additional operations. In recent decades, research on biodegradable biomedical metallic materials has largely concentrated on magnesium-based alloys[1–9] and iron-based alloys[10–15]. However, both alloy types face challenges that hinder their clinical application. Magnesium-based alloys often deteriorate too rapidly, compromising their therapeutic efficacy before achieving the desired results. Conversely, iron-based alloys typically require follow-up surgeries to extract implants because of their slow degradation[12], thus undermining the benefits associated with degradable materials. In contrast to iron and magnesium, zinc possesses a standard electrode potential of −0.763 V[16], which is situated between magnesium and iron[16], thus exhibiting an intermediate degradation rate. However, the hexagonal close-packed lattice structure of Zn, characterized by restricted slip systems, results in relatively inferior mechanical properties[17–18], significantly restricting the use and advancement of this material.

Currently, many researchers have enhanced the mechanical characteristics of zinc alloys by adding alloying elements, particularly those relevant to human nutrition. For example, tin (Sn) is an essential trace element that supports growth and is found in various human organs and tissues. Gu et al[19] examined the corrosion and mechanical properties of Mg-1Sn, concluding that Sn serves as an excellent alloying agent.

Received date: November 30, 2025
Foundation item: National Natural Science Foundation of China (82205308)
Corresponding author: Zhao Linlin, Ph. D., Associate Professor, School of Materials Science and Engineering, Tianjin University of Technology, Tianjin 300384, P. R. China, E-mail: luxingzhao@hotmail.com; Zhang Xin, Ph. D., Professor, School of Materials Science and Engineering, Tianjin University of Technology, Tianjin 300384, P. R. China, E-mail: zhangxin3510110@tjut.edu.cn

Research has demonstrated that incorporating Sn can significantly enhance the mechanical properties of zinc alloys[19–20], although their cellular compatibility remains suboptimal. This study aims to enhance the biocompatibility of Zn-Sn alloys through alloying. Strontium (Sr) is identified as a vital nutrient for the human body and a fundamental element of bone tissue, making it a promising alloying component for biodegradable orthopedic materials. Previous investigations have indicated that adding Sr can improve the biocompatibility of zinc alloy[20] without adversely affecting its mechanical properties[21]. This study presented the design of Zn-1.5Sn-*x*Sr ternary alloys with varying Sr levels and evaluated their microstructures, mechanical properties, corrosion resistance, and biocompatibility.

2 Experiment

2.1 Materials

The pure Zn (99.9%), pure Sn (99.9%), and pure Sr (99.9%) were mixed together. Before melting, due to the high tendency of Sr to oxidize and release hydrogen when exposed to water, a vacuum sealing experiment was performed under an Ar protective atmosphere. The VS-Q2 vacuum sealing machine was selected to seal the sample tubes and isolate oxygen. Meanwhile, the mixture was then melted into an alloy using a muffle furnace (SGM. M25/10At) at a temperature range of 800–900 °C. After cooling to room temperature, a heat treatment process was further conducted, which primarily involved low-temperature annealing. The alloy was heated to the annealing temperature (250 °C), held for 5 h, and followed by air cooling to room temperature. Additionally, a solution treatment was performed, where the alloy was heated to 365 °C for 7 h, and then rapidly cooled to allow for uniform dissolution of alloy elements and the formation of fine precipitated phases, enhancing the strength and wear resistance of alloy. Each sample had a mass of 50 g.

2.2 Microstructure characterization

The metallographic analysis of alloy samples with different compositions was performed using an optical microscope (OM, BX53M). In the X-ray diffraction (XRD, D8 ADVANCE) experiment, Cu Kα radiation was selected as the radiation source to analyze the phase composition of a series of zinc alloy samples. The operating acceleration voltage was set at 40 kV, and the current was 20 mA. Data were collected in a continuous mode within the range of 2θ=20°–100° with a step size of 0.4° and a dwell time of 3 s.

Concurrently, scanning electron microscope (SEM, Thermo Fisher Phenom), energy-dispersive spectroscope (EDS), and transmission electron microscope (TEM) were used for microstructural analysis on the vertical surface of the samples. Before this, the heat-treated samples were cut into smaller pieces of 4 mm×4 mm×2 mm or 8 mm×8 mm×2 mm in dimension using an electric spark wire cutting machine (DK7750). These pieces were then ground using SiC sandpapers with grit sizes of 400#, 800#, 1500#, 2000#, and 4000#, followed by polishing using a polishing machine with 1.0–1.5 μm alumina paste. After polishing, the surfaces were etched with a solution of anhydrous ethanol and nitric acid, washed with water, and dried. The chemical composition and microstructure of the corrosion products were analyzed using EDS on a JSM 7800F SEM. Scanning analysis was performed using an FEG Quanta three-dimensional FEI SEM instrument, with the magnification set to 100–500× before immersion and 5 000–10 000× after immersion.

2.3 Mechanical property test

The cut cylindrical samples (Φ3 mm×5 mm) were placed in an AGS-X universal mechanical testing machine for compression fracture experiments. All samples were ground with 4000# SiC sandpaper. Vickers hardness was measured using a hardness tester (HMV-2T, Shimadzu Corporation, Japan) with a 100 g load applied for 15 s. Six indentations were made on each sample, and the diagonal lengths of the indentations were measured using a calibrated micrometer attached to the microscope eyepiece. The Vickers hardness number HV was calculated using the formula $HV=1.8544P/d^2$, where HV denotes the Vickers hardness value, P is the indenter load in kg, and d is the diagonal length of the indentation in mm.

2.4 Electrochemical test

The electrochemical test was performed according to the ASTM G102-89 standard. A three-electrode system was employed, with a saturated calomel electrode (SCE) as the reference electrode, a platinum electrode as the counter electrode, and the alloy sample under test as the working electrode. The electrochemical test environment was simulated body fluid (SBF), and a CHI660E electrochemical workstation was used for the electrochemical tests. The open-circuit potential (OCP) and polarization curve (Tafel) of the alloys in SBF solution were measured. The experimental data were processed using CHI660E for fitting and obtaining additional electrochemical parameters.

2.5 Immersion test

Immersion tests were performed in SBF according to the ASTM G31-72 standard to simulate the degradation process of the alloy in vivo. The polished and etched samples, which were previously weighted using an electronic balance (Mettler Toledo, MS204S), were immersed in SBF for 7 and 14 d, with the initial mass recorded as M_0. The surface corrosion morphology and corrosion products were observed using SEM. To remove the corrosion products, an NH_4Cl solution in deionized water of 100 g/L was used. When a large number of bubbles appeared on the sample surface, the sample was immediately removed, rinsed with deionized water, dehydrated with anhydrous ethanol, and then dried. The samples were then weighed using an electronic balance, and the average mass of three measurements was taken as the final mass (M). The mass loss rate is calculated by $[(M_0-M)/M_0]\times100\%$.

2.6 Cell viability test

Cell culture experiments were conducted on the leachates of five different zinc alloy compositions using Dulbecco ' s modified Eagle medium (DMEM) supplemented with 10%

fetal bovine serum and 1% penicillin-streptomycin to evaluate their biocompatibility. The undiluted leachate was used as a stock solution (100%), and a series of diluted solutions at concentrations of 10%, 20%, 40%, 60%, and 80% was prepared. The extraction ratio was 3 cm^2/mL, L293 cells (1×10^4 cells per well) were seeded onto 96-well plates in 200 μL DMEM and allowed to attach for 24 h. After cell attachment, the medium was replaced with 100 μL of leachates at a series of concentrations. The plates were incubated in a humidified atmosphere at 37 °C with 5% CO_2 for 24, 48, and 72 h. The cell viability was evaluated by 3-(4,5-dimethylthiazol-2-yl)-2,5-diphenyltetrazolium bromide (MTT) assay. The presented data are averaged results of quadruplicate experiments. The optical density (OD) of each well indirectly reflected the number of viable cells, and the cell viability (CV) was calculated using the following formula: CV=(experimental average OD/negative control average OD)×100%.

3 Results

3.1 XRD analysis

XRD patterns in Fig. 1 illustrate that no solid solution formed in alloys with varied compositions, which is mainly attributed to the fact that Sn predominantly manifests as Sn-rich phases within the alloys, exhibiting very low solid solubility[22]. In XRD patterns, the Zn diffraction peaks appear most prominently, followed by the Sn diffraction peaks. Furthermore, the diffraction peak of the minor secondary phase, $SrZn_{13}$, is also exhibited. Its peak intensity is very weak, which may be due to the very low volume fraction or small size of $SrZn_{13}$ phase in the matrix. As shown in Fig. 1, when the Sr addition ranges from 0.3wt% to 0.5wt%, a small amount of primary $SrZn_{13}$ phase preferentially forms at approximately 600 °C during the cooling process. As the temperature decreases to 420 °C, a stable $SrZn_{13}$ phase structure is established. Upon further cooling below 419.58 °C, the primary η-Zn phase precipitates. Solidification terminates with the formation of a microstructure consisted of η-Zn and $SrZn_{13}$ particles, which is consistent with XRD results[23–26].

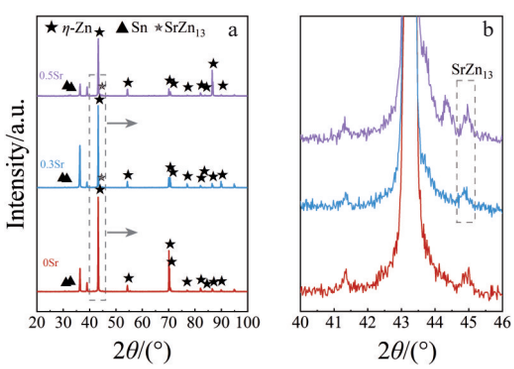

Fig.1 XRD patterns of Zn-1.5Sn-*x*Sr alloys with different compositions

3.2 SEM and EDS analysis

In Fig.2, SEM images reveal two distinct phases: one is the gray matrix phase and the other is a white phase aggregated at the grain boundaries. According to EDS results, the matrix phase is the η-Zn phase, whereas the Sn-rich phase is aggregated at the grain boundaries. The secondary phase $SrZn_{13}$ accumulates at the grain boundaries, intersecting with the matrix phase. To analyze the composition and the secondary phase of the alloy, EDS analysis was conducted on the highlighted areas (yellow boxes marked in Fig. 2). Table 1 details the compositions of each highlighted area. The matrix at location 1 predominantly consists of Zn with a small amount of Sn. The secondary phase at the grain boundaries (location 2) mainly contains a Sn-rich phase, with a less amount of Zn. With the addition of element Sr, it mainly aggregates at the grain boundaries.

3.3 Grain size analysis

Fig. 3 displays OM images of Zn-1.5Sn, Zn-1.5Sn-0.3Sr, and Zn-1.5Sn-0.5Sr alloys, along with the size distribution histograms of $SrZn_{13}$ phases and grains. As shown in Fig.3d–3e, the addition of 0.3wt% Sr to the Zn-1.5Sn alloy results in significant microstructural refinement, with the average grain size markedly decreasing from 61.3 μm to 40.8 μm. In Fig.3f, when the Sr content increases to 0.5wt%, the grain size further reduces from 40.8 μm to 37.8 μm. This refinement can be attributed to the formation of $SrZn_{13}$ particles induced by the Sr addition, which effectively inhibits the growth of η-Zn grains. Conversely, Fig. 3g – 3h reveal that the higher Sr content corresponds to an increased size of the secondary phase particles, which is consistent with the facilitated growth of the $SrZn_{13}$ phase.

3.4 TEM analysis

Fig. 4 presents the bright-field (BF) -TEM image and the corresponding selected-area electron diffraction (SAED) pattern of the Zn-1.5Sn-0.5Sr alloy. The SAED pattern in Fig. 4b confirms that the precipitate is $SrZn_{13}$ phase, which

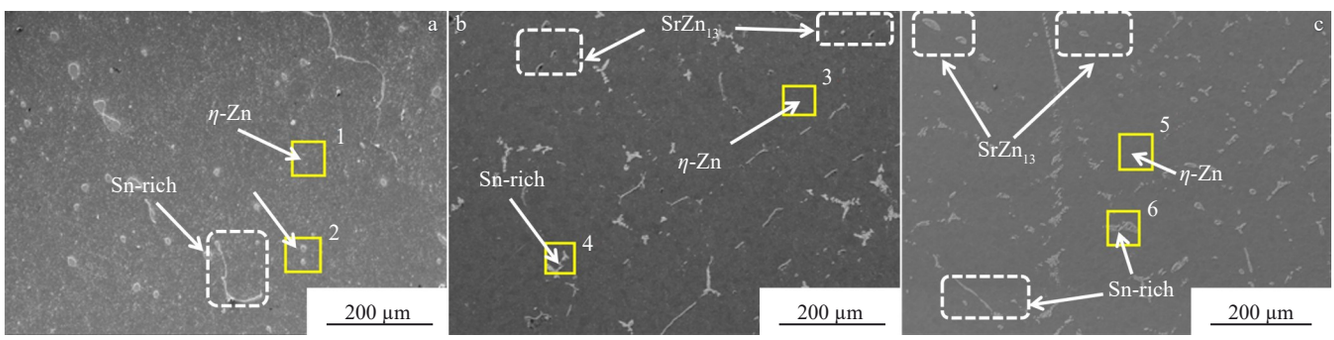

Fig.2 SEM images of Zn-1.5Sn-*x*Sr alloys with different compositions: (a) *x*=0, (b) *x*=0.3, and (c) *x*=0.5

Table 1 EDS results of different locations of Zn-1.5Sn-*x*Sr alloys marked in Fig.2 (at%)

Alloy	Location	Zn	Sn	Sr
Zn-1.5Sn	1	99.96	0.04	-
	2	8.39	91.96	-
Zn-1.5Sn-0.3Sr	3	99.14	0.83	0.03
	4	40.43	57.41	2.16
Zn-1.5Sn-0.5Sr	5	98.80	0.81	0.39
	6	4.08	95.29	0.63

crystallizes in the cubic $NaZn_{13}$-type structure (space group Fm-3c)[23]. Calculation results indicate that the lattice parameters are $a=b=c=1.218$ nm.

3.5 Mechanical properties

Mechanical property tests were performed on Zn-1.5Sn-*x*Sr alloys. Table 2 displays the calculated yield strength and elastic modulus, which were obtained from the Fig. 5. The addition of Sr enhances the yield strength because of the secondary-phase strengthening and fine-grain strengthening. In comparison to other alloy types, the yield strength of Zn alloys closely aligns with that of natural bone, which ranges from 50 MPa to 150 MPa[22,27]. Especially for the cancellous bone of the human femoral head or tibia, the yield strength is only 20.7–99.7 MPa[28–29]. Moreover, the strength of the implant, which is consistent with that of the studied Zn-Sn-Sr alloy, must be more than three times that of the human bone. The elastic modulus of the alloys remains relatively stable, with the Zn-1.5Sn-0.5Sr alloy exhibiting the maximum elastic modulus at 1.64 GPa, coupled with a peak yield strength of 100.6 MPa. In addition, the study results match the range of elastic modulus for tibial cancellous bone reported in previous studies[30–31], which is approximately 0.2–1.3 GPa. To a certain extent, it reduces the possibility of stress shielding effects[22,27].

3.6 Electrode polarization analysis

The polarization curves illustrated in Fig.6a indicate that as the current density increases, distinct potential platforms emerge at the electrodes. This phenomenon suggests the development of a passive film on the material surface. With a further increase in current density, the curves exhibit bulges, indicating that the passive film is compromised, leading to pitting corrosion. Among the tested alloys, Zn-1.5Sn-0.3Sr exhibits higher corrosion resistance than the others. Table 3 presents the electrochemical parameters derived from Fig. 6. The corrosion potential and current density of Zn-Sn-0.3Sr alloy are − 1.161 V and 44.40 μA/cm^2, respectively. The degradation rate reaches 0.519 mm/a. It is evident that with a higher Sr content, the corrosion rate of the Zn-1.5Sn-0.3Sr alloy remains the lowest. This effect arises primarily because that the standard electrode potential of Sr (−2.89 V) exceeds that of Zn (− 0.76 V), thereby improving the corrosion resistance of the alloy. When the Sr content reaches 0.3wt%,

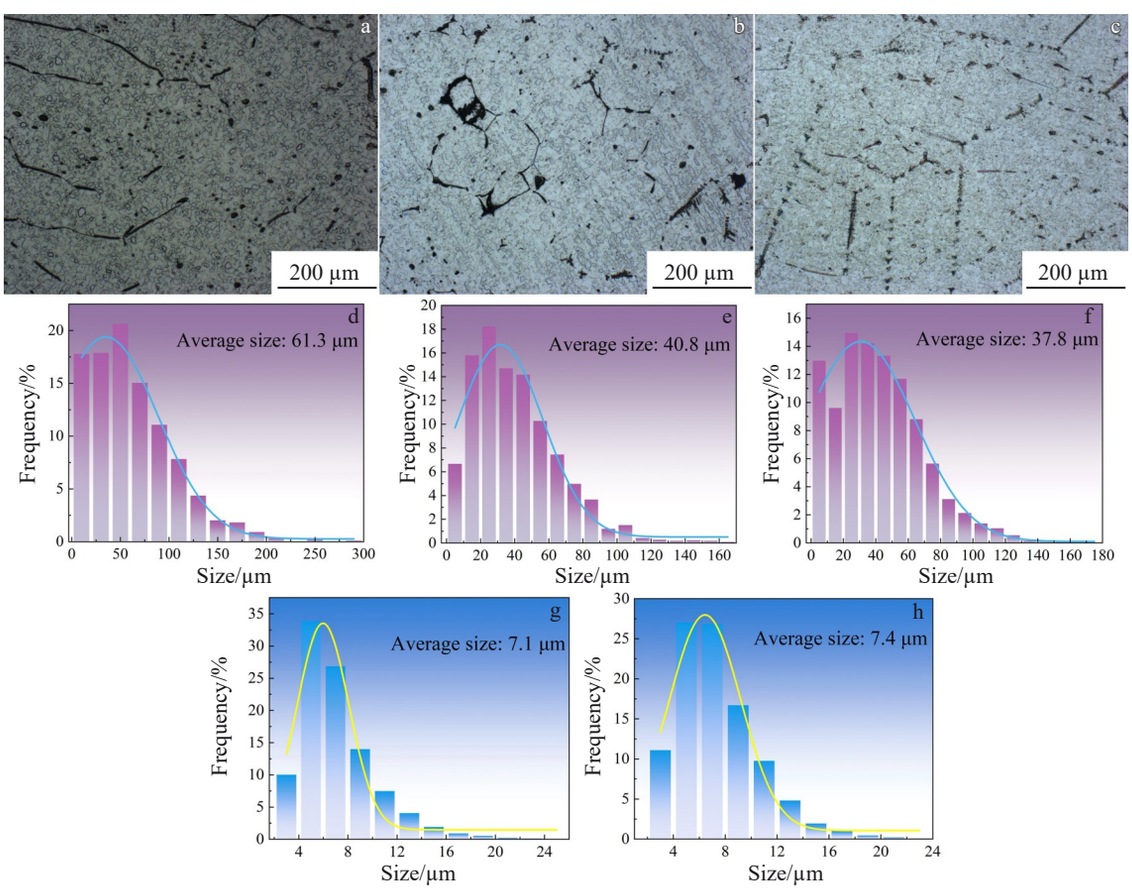

Fig.3 OM images (a–c), grain size distribution histograms (d–f), and size distribution histograms of secondary phases (g–h) of Zn-1.5Sn-*x*Sr alloys with different compositions: (a, d) $x=0$, (b, e, g) $x=0.3$, and (c, f, h) $x=0.5$

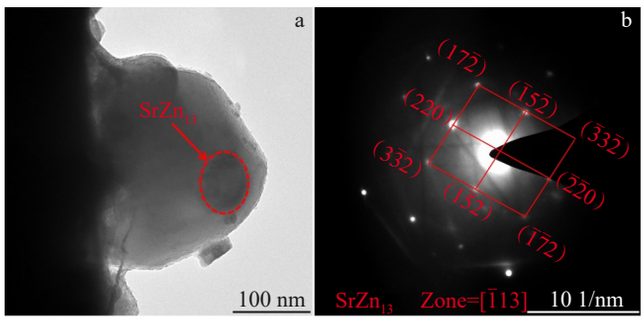

Fig.4 BF-TEM image of Zn-1.5Sn-0.5Sr alloy (a) and SAED pattern of the circled area marked in Fig.4a (b)

Table 2 Yield strength and elastic modulus of Zn-1.5Sn-*x*Sr alloys

Alloy	Yield strength/MPa	Elastic modulus/GPa
Zn-1.5Sn	47.7±1.6	1.17±0.15
Zn-1.5Sn-0.3Sr	51.5±1.8	1.10±0.11
Zn-1.5Sn-0.5Sr	100.6±2.4	1.64±0.18

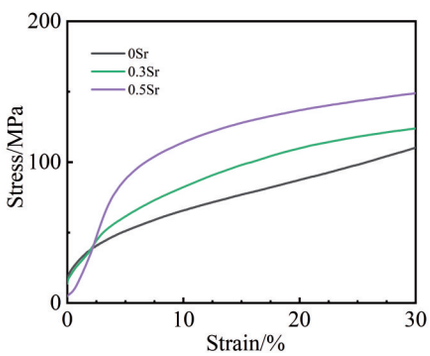

Fig.5 Stress-strain curves of Zn-1.5Sn-*x*Sr alloys

the corrosion rate decreases. This may be attributed to the galvanic corrosion that occurs because of the potential difference between Sr and Zn. When the Sr content is low, corrosion products accumulate on the surface, forming a passive film that prevents further corrosion[22]. However, as the Sr content continues to increase, the number of galvanic corrosion sites also increases, leading to the particle destruction of the passive films, thereby reducing the corrosion resistance[32]. The mass loss rate curves shown in Fig.6b demonstrate that the addition of Sr slows the mass loss rate in comparison to the Zn-Sn matrix alloy, which is due to the formation of a dense oxide film from SrO and SnO_2 on the alloy surface. This oxide film reduces corrosion in the matrix,

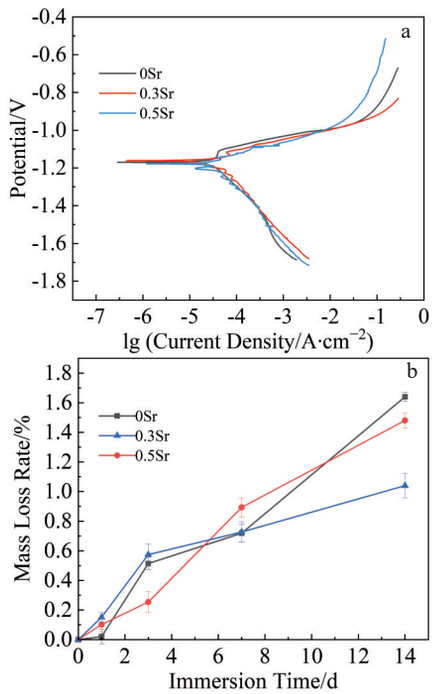

Fig.6 Polarization curves (a) and mass loss rates (b) of Zn-1.5Sn-*x*Sr alloys

leading to fewer corrosion products on the surface layer.

3.7 Immersion test analysis

Fig. 7 shows the corrosion morphologies of alloys with varying compositions after immersion in SBF for both 7 and 14 d. After 7 d, localized corrosion manifests on the surface of the alloy, with Zn-1.5Sn-0.5Sr showing the most significant corrosion damage. After 14 d, the alloys exhibit localized degradation and severe pitting corrosion morphology. This phenomenon may occur because of the formation of a thin, dense protective film on the Zn-Sn-*x*Sr alloy surface, facilitated by a small amount of Sr. Over the immersion period, this protective film gradually evolves into a thicker layer integrated with corrosion products, thereby mitigating localized corrosion. In contrast, the alloys with higher Sr concentration demonstrate a loose, porous film structure that fails to adequately protect the corroding surface, leading to general corrosion.

X-ray photoelectron spectroscopy (XPS) spectra of Zn 2p, Sn 3d, Sr 3d, C 1s, O 1s, and P 2p are shown in Fig. 8. According to previous researches[33–39], the components of the passive film formed by the degradation of the Zn matrix in SBF mainly include ZnO, $Zn(OH)_2$, and $ZnCO_3$, probably containing $Zn_3(PO_4)_2 \cdot 2H_2O$ and $Zn_5(CO_3)_2(OH)_6$ due to the

Table 3 Electrochemical parameters of Zn-1.5Sn-*x*Sr alloys

Alloy	Corrosion potential, E_{corr}/V	Corrosion current density, I_{corr}/μA·cm^{-2}	Polarization resistance, R_p/kΩ·cm^{-2}	Constant phase element, CPE/×10^{-4} Ω^{-1}·cm^{-2}·s^n	Corrosion rate/ mm·a^{-1}
Zn-1.5Sn	−1.170	48.27	3.623	4.674	0.565
Zn-1.5Sn-0.3Sr	−1.161	44.40	8.979	16.33	0.519
Zn-1.5Sn-0.5Sr	−1.178	62.72	1.519	6.800	0.734

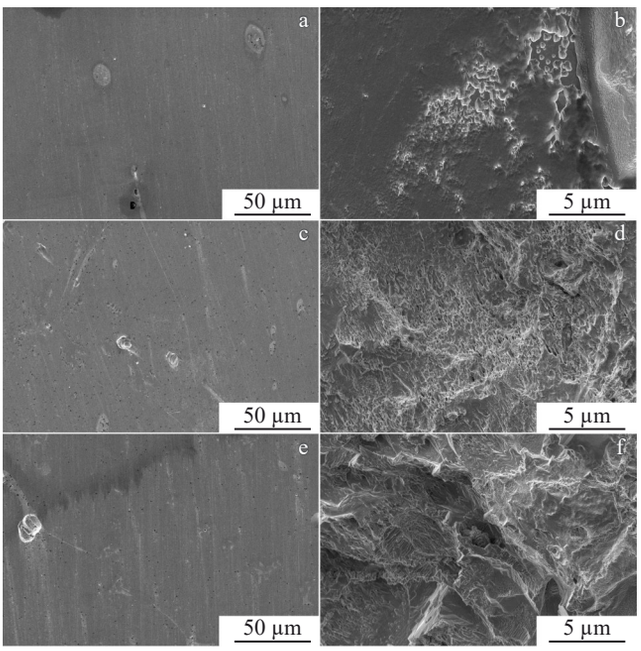

Fig.7 Corrosion morphologies of Zn-1.5Sn-*x*Sr alloys immersed for 7 (a, c, e) and 14 (b, d, f) d: (a–b) *x*=0, (c–d) *x*=0.3, and (e–f) *x*=0.5

introduction of impurities, such as foreign CO_2. The Zn 2p spectrum indicates that ZnO, a corrosion-resistant component, and $Zn(OH)_2$ are detected at photoelectron binding energies of 1021.9 and 1022.7 eV, respectively. Moreover, the content ratio of ZnO to $Zn(OH)_2$ is approximately 1: 0.85. SnO_2 is detected at an electron binding energy of approximately 486.2 eV, which is also identified in the respective XPS spectra and is in agreement with existing research[40–41]. Furthermore, as a component of the passive film, Sr tends to form two species, SrO and $Sr(OH)_2$[42]. The Sr 3d spectral peak is detected for Sr^{2+} at a binding energy of approximately 133.2 eV. C 1s and P 2p spectra show that CO_3^{2-} and PO_4^{3-} are detected at electron binding energies of 286.2 and 133.8 eV, respectively. In C 1s spectra, the content ratio of C to CO_3^{2-} is about 1:0.14. The spectrum of O 1s is decomposed into three contributions at 531.2, 532.0, and 531.8 eV, which are related to OH^-, O^{2-}, and the average binding energies for PO_4^{3-} and CO_3^{2-}, respectively[43–44]. The content ratio of OH^- to O^{2-} is approximately 0.79: 1. Integrating the above analysis and previous studies[45], it can be concluded that the composition of the passive film formed by the corrosion products includes $Zn(OH)_2$, $ZnCO_3$, $Zn_3(PO_4)_2 \cdot 2H_2O$, and $Zn_5(CO_3)_2(OH)_6$, as well as a small amount of ZnO formed by the dehydration of $Zn(OH)_2$, the passive film contains a small amount of SnO_2, SrO, and their hydroxides.

3.8 Biocompatibility

Fig.9 illustrates the biocompatibility of various alloys with different concentrations of extract solutions cultured for varying durations. The dose-dependent cytotoxic effects of the extract solutions of different alloys were examined. The incorporation of element Sr will cause the alloy to release Sr^{2+} during the degradation process in SBF, which promotes the proliferation and differentiation of osteoblasts, thereby achieving the purpose of bone tissue repair[46–47]. As shown in Fig.9, when the concentration of the extract solution is low (≤ 20%), all alloys exhibit relatively good cell survival rates with longer culture durations. Moreover, at excessively high concentrations of the extract solution (≥60%), the alloys with 0.5wt% Sr present significant cytotoxic effects. Overall, Zn-1.5Sn-0.3Sr alloy demonstrates superior biocompatibility, with cell viability approaching 130% when the alloy is cultured at a concentration of 10% for 72 h.

As shown in Fig. 10, a majority of cells exhibit a spindle-shaped morphology, while a small proportion of cells exhibit round or pancake-shaped morphology. The above results indicate the good cytocompatibility of Zn-1.5Sn-0.3Sr alloy.

4 Discussion

In order to extend the application of zinc alloys to the biomedical field, various alloying elements (Mg, Ca, Li, Mn, Cu, and Ag) have been added to improve mechanical properties[48]. In this study, as-cast Zn-1.5Sn-*x*Sr (*x*=0, 0.3, 0.5, wt%) alloys were selected. Characterization by XRD and SEM reveals that the alloys mainly consist of η-Zn and Sn-rich phases, along with minor amounts of $SrZn_{13}$. The introduction of Sr promotes fine-grain strengthening, leading to an enhancement in mechanical properties. Besides, the yield strength of alloys with similar composition was compared, as shown in Table 4[23,25,49].

By analyzing the passive potential, corrosion current density, and corrosion rate of the three alloys, the alloy with 0.3Sr is the closest to the standard requirements for mechanical implants, that is, the degradation rate is no greater than 0.5 mm/a[50].

Through the analysis of the corrosion morphology of several alloys after immersion, it can be observed that with the increase in Sr content, the pitting corrosion traces on the Zn alloy become more severe. This may be due to the potential difference between Zn and Sr, leading to micro-galvanic corrosion. After 14 d, the material transitions from localized corrosion to general corrosion, with distinct corrosion pits. By analyzing XPS spectra of Zn, Sn, Sr, O, C, and P collected from each alloy, along with previous research, the corrosion products include $Zn(OH)_2$, ZnO, and trace SnO_2 and SrO, with CO_3^{2-} and PO_4^{3-} also involved in the corrosion product layers. The degradation process of Zn alloy in SBF can generally be described by the following reactions[51]:

$$Zn \rightarrow Zn^{2+} + 2e^- \text{ (anode reaction)} \quad (1)$$

$$2H_2O + O_2 + 4e^- \rightarrow 4OH^- \text{ (cathode reaction)} \quad (2)$$

$$Zn^{2+} + 2OH^- \rightarrow Zn(OH)_2 \quad (3)$$

$$Zn^{2+} + 2OH^- \rightarrow ZnO + H_2O \quad (4)$$

The aforementioned reactions can also be explained using the schematic diagram in Fig.11. In the first stage, as shown in Fig. 11a, metallic Zn at the anode loses electrons and transforms into Zn^{2+}, while oxygen and water at the cathode gain electrons to form OH^-. In the second stage, as illustrated in Fig. 11b, the OH^- generated at the cathode reacts with the Zn^{2+} generated at the anode to form insoluble hydroxide,

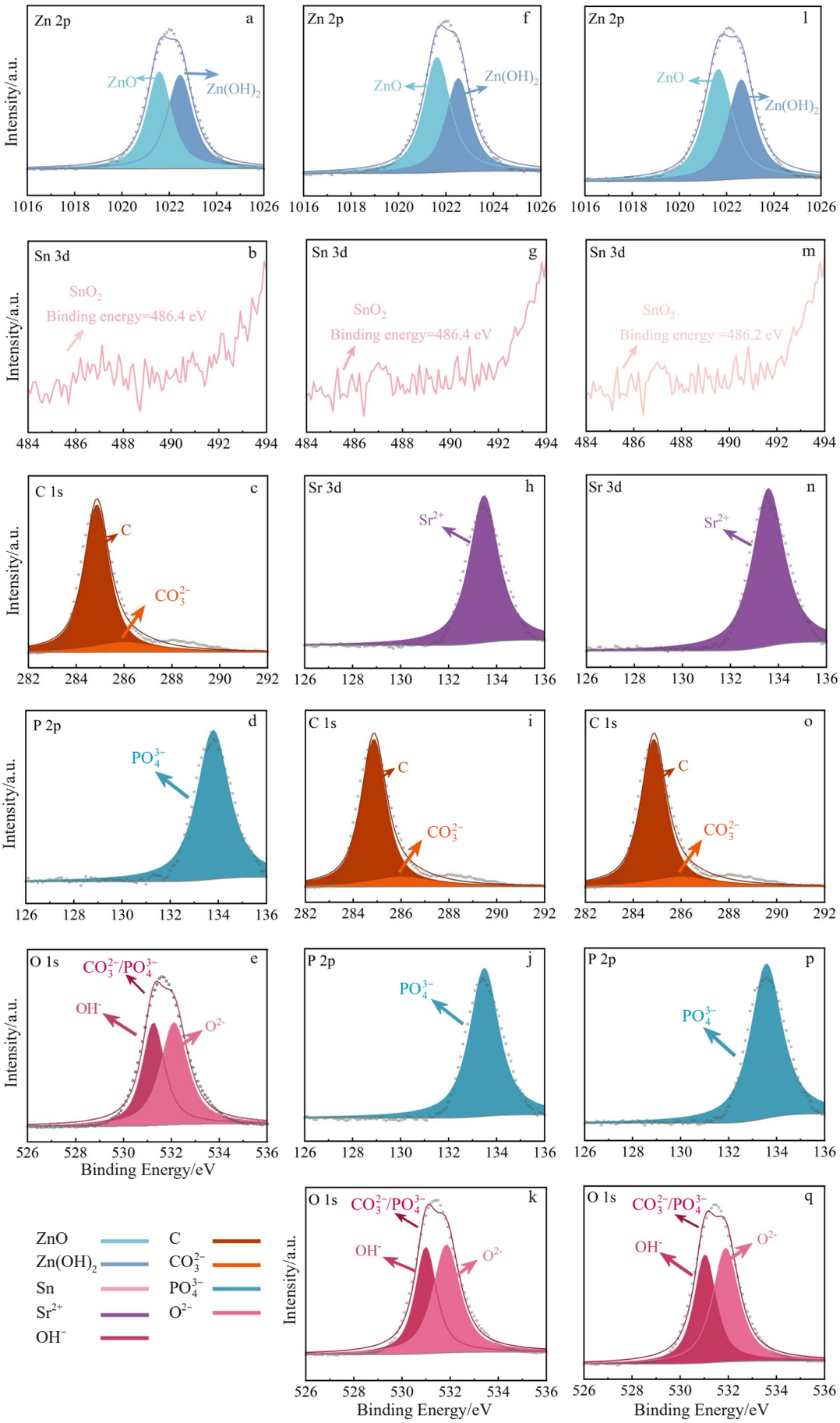

Fig.8 XPS valence spectra of Zn-1.5Sn-*x*Sr alloys after immersion: (a–e) *x*=0, (f–k) *x*=0.3, and (l–q) *x*=0.5

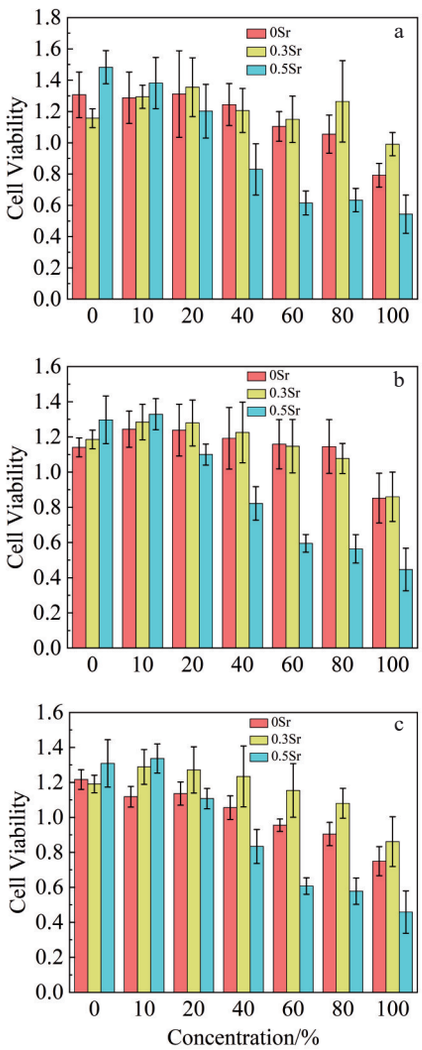

Fig.9 Histograms of in vitro cytotoxicity assay of different alloys with varying concentrations of extract solutions cultured for 24 h (a), 48 h (b), and 72 h (c)

which accumulates and forms a protective layer on the surface of the substrate. In the third stage, as depicted in Fig. 11c,

Table 4 Yield strength of alloys with similar compositions[23,25,49]

As-cast alloy	Yield strength/MPa
Zn-Sn-Sr	52±1.8
Zn-Sr[23]	74±3.2
Zn-Fe[25]	65±5.5
Mg-Zn-Sr[49]	62±3.5

under alkaline conditions, Cl^- present in SBF can react with $Zn(OH)_2$ to form soluble $ZnCl_2$, which compromises the stability of the passive film[52]. This is due to the small radius and high chemical activity of Cl^-, which often penetrates the pores in the corrosion product film[53], exposing the underlying substrate as a small anode and the intact corrosion product film as a cathode region, thereby forming a micro-galvanic cell that accelerates the corrosion of Zn. As the corrosion process continues, a portion of the hydroxides undergoes dehydration to form oxides. This transformation promotes the formation of a new calcium-phosphate compound layer on the top of the original hydroxide layer, which also contains small amounts of carbonate and phosphate crystals. Under weakly alkaline conditions, this compound further transforms into hydroxyapatite[51,54], which can be used to evaluate the bioactivity of the material, as illustrated in Fig.11d.

Table 5 summarizes the cell viability obtained from MTT assays of Zn-Sr alloys with similar composition at a 10% extract concentration[23,55]. According to ISO 10993-5[56], these results meet the requirement for cell viability greater than 75%, indicating good biocompatibility. Based on the data, such as corrosion rate and cell viability, it is determined that the optimal Sr addition range is 0–0.3wt%. Excessive Sr can accelerate the release of Zn^{2+} during the degradation of the alloy in bodily fluids, leading to reduced cell tolerance and compromising the stability of Zn-based implants. Li et al[57] found that adding elements Mg and Ca to Zn-Mn alloys can effectively enhance cellular tolerance to excessive Zn^{2+}.

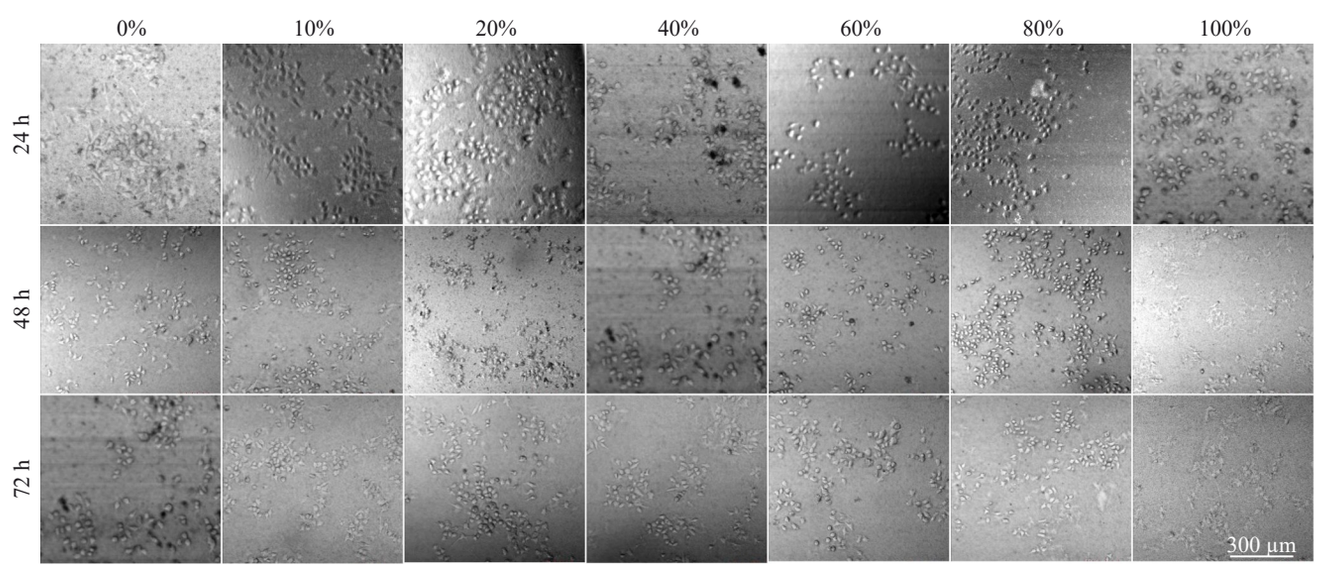

Fig.10 Cell morphologies of Zn-1.5Sn-0.3Sr alloy with varying concentrations of extract solutions after MTT experiments for 24, 48, and 72 h

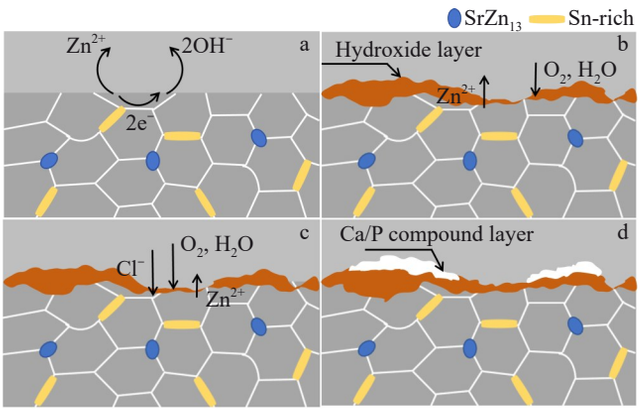

Fig.11 Schematic diagrams of surface degradation of Zn-Sn-Sr alloy

Table 5 Cell viability obtained from MTT assays of Zn-Sr alloys with similar composition[23,55]

Alloy	Cell viability/%
Zn-Sn-Sr	120±11.2
Zn-Sr[23]	80±2.7
Mg-Zn-Mn-Sr[57]	102±8.6

5 Conclusions

1) The introduction of Sr leads to the grain refinement of Zn-Sn alloy by the formation of the $SrZn_{13}$ phase. The presence of the $SrZn_{13}$ phase inhibits grain boundary movement while providing nucleation sites for new phases, and also creates favorable conditions for enhancing the corrosion resistance of the alloy.

2) The Zn-Sn alloy with 0.5wt% Sr exhibits better comprehensive performance. The yield strength and elastic modulus reach 100.6 MPa and 1.64 GPa, respectively.

3) The corrosion potential and current density of Zn-Sn-0.3Sr alloy are −1.161 V and 44.40 μA/cm^2, respectively. The degradation rate reaches 0.519 mm/a.

4) The degradation products of the Zn-Sn-0.3Sr alloy in SBF primarily consist of zinc oxides and hydroxides. In addition, oxides of Sn and Sr, as well as small amounts of carbonate and phosphate crystals, are observed.

5) When the extract concentration of the component does not exceed 20%, the cells cultured for 72 h grow well, showing great potential for application. MTT experiments show that the cell viability of Zn-1.5Sn-0.3Sr alloy can reach up to 130%.

References

1 Agarwal S, Curtin J, Duffy B *et al*. *Biodegradable Magnesium Alloys for Orthopaedic Applications*[J], 2016, 68: 948

2 Sanchez A H M, Luthringer B J C, Feyerabend F *et al. Acta Biomaterialia*[J], 2015, 13: 16

3 Chen Y J, Xu Z G, Smith C *et al. Acta Biomaterialia*[J], 2014, 10(11): 4561

4 Gu X N, Zheng Y F. *Frontiers of Materials Science in China*[J], 2010, 4(2): 111

5 Staiger M P, Pietak A M, Huadmai J *et al. Biomaterials*[J], 2006, 27(9): 1728

6 Witte F. *Acta Biomaterialia*[J], 2010, 6(5): 1680

7 Walker J, Shadanbaz S, Woodfield T B F *et al. Journal of Biomedical Materials Research Part B: Applied Biomaterials*[J], 2014, 102(6): 1316

8 Song Jie, Ding Hao, Ding Hongyan *et al. Rare Metal Materials and Engineering*[J], 2023, 52(10): 3539 (in Chinese)

9 Zhang Y, Liu W, Liu Y *et al. Rare Metal Materials and Engineering*[J], 2023, 52(9): 3065

10 Schinhammer M, Hänzi A C, Löffler J F *et al. Acta Biomaterialia*[J], 2010, 6(5): 1705

11 Francis A, Yang Y, Virtanen S *et al. Journal of Materials Science: Materials in Medicine*[J], 2015, 26(3): 138

12 Hermawan H, Dubé D, Mantovani D. *Advanced Materials Research*[J], 2006, 15–17: 107

13 Huang T, Cheng J, Zheng Y F. *Materials Science and Engineering C*[J], 2014, 35: 43

14 Moravej M, Mantovani D. *International Journal of Molecular Sciences*[J], 2011, 12(7): 4250

15 Moszner F, Sologubenko A S, Schinhammer M *et al. Acta Materialia*[J], 2011, 59(3): 981

16 Lu Y, Bradshaw A R, Chiu Y L *et al. Materials Science and Engineering C*[J], 2015, 48: 480

17 Ke G, Yue R, Huang H *et al. Transactions of Nonferrous Metals Society of China*[J], 2020, 30(7): 1873

18 Wang H, Zhang Y, Cai H *et al. Materials Letters*[J], 2024, 360: 136037

19 Gu X N, Zheng Y F, Cheng Y *et al. Biomaterials*[J], 2009, 30(4): 484

20 Li H F, Xie X H, Zheng Y F *et al. Scientific Reports*[J], 2015, 5(1): 10719

21 Yang H T, Jia B, Zhang Z C *et al. Nature Communications*[J], 2020, 11(1): 401

22 Guo P, Bagheri R, Yang L *et al. Materials and Corrosion*[J], 2021, 73(2): 231

23 Qiao H, Li Q, Zhang J *et al. Materials Chemistry and Physics*[J], 2025, 338: 130664

24 Liu J, Linsley C S, Su Y *et al. ACS Applied Materials & Interfaces*[J], 2024, 16(38): 50125

25 Guan Z, Linsley C S, Pan S *et al. Metallurgical and Materials Transactions A*[J], 2020, 51(9): 4406

26 Guan Z, Linsley C S, Pan S *et al. ACS Biomaterials Science & Engineering*[J], 2021, 8(1): 328

27 Ji C W, Ma A B, Jiang J H *et al. Journal of Alloys and Compounds*[J], 2024, 993: 174669

28 Wang L, Chen Q, Yarlagadda P K D V *et al. Materials & Design*[J], 2021, 209: 109986

29 Yang S, Leong K F, Du Z *et al. Tissue Engineering*[J], 2001, 7(6): 679

30 Bo L, Cheng X, Wei L *et al. Acta of Bioengineering and Biomechanics*[J], 2021, 23(3): 97

31 Hobatho M C, Rho J Y, Ashman R B. *Journal of Biomechanics*[J], 1997, 30(8): 837

32 Chen K, Gao S, Gu X N *et al. Biomaterials*[J], 2025, 321: 123343

33 Klein J. *Journal of Catalysis*[J], 1983, 82(2): 424

34 Dake L S, Baer D R, Zachara J M. *Surface and Interface Analysis*[J], 1989, 14(1–2): 71

35 Barr T L, Yin M, Varma S. *Journal of Vacuum Science & Technology A: Vacuum, Surfaces, and Films*[J], 1992, 10(4): 2383

36 Schön G. *Journal of Electron Spectroscopy and Related Phenomena*[J], 1973, 2(1): 75

37 Strohmeier B. *Journal of Catalysis*[J], 1984, 86(2): 266

38 Deroubaix G, Marcus P. *Surface and Interface Analysis*[J], 1992, 18(1): 39

39 Li Z, Shi Z Z, Hao Y *et al. Materials Science and Engineering C*[J], 2020, 114: 111049

40 Li H F, Yu H T, Zheng Y F *et al. Materials & Design*[J], 2015, 83: 95

41 Yang Y Y, Liu Y Y, Cheng M L *et al. Acta Metallurgica Sinica* (*English Letters*)[J], 2018, 32(1): 98

42 Yu B W, Jiang H T, Zhang Y. *Journal of Power Sources*[J], 2024, 602: 234269

43 Yang L, Hort N, Laipple D *et al. Acta Biomaterialia*[J], 2013, 9(10): 8475

44 Diler E, Lescop B, Rioual S *et al. Corrosion Science*[J], 2014, 79: 83

45 Wang Z, Zhang Q, Bagheri R *et al. Journal of Materials Science & Technology*[J], 2019, 35(11): 2705

46 Su Y C, Fu J Y, Du S K *et al. Smart Materials in Medicine*[J], 2022, 3: 117

47 Liu Y, Yin Z, Liu Y *et al. International Journal of Electrochemical Science*[J], 2018, 13(2): 1640

48 Bowen P K, Shearier E R, Zhao S *et al. Advanced Healthcare Materials*[J], 2016, 5(10): 1121

49 Gerashi E, Alizadeh R, Mahmudi R. *Journal of Materials Research and Technology*[J], 2022, 22: 63

50 Hammam R E, Abdel-Gawad S A, Moussa M E *et al. International Journal of Metalcasting*[J], 2023, 17(4): 2794

51 Alves M M, Prošek T, Santos C F *et al. RSC Advances*[J], 2017, 7(45): 28224

52 Jain D, Pradhan S, Singh S K *et al. Canadian Metallurgical Quarterly*[J], 2023, 63(4): 1325

53 Cubides Y, Su S S, Castaneda H. *Corrosion*[J], 2016, 72(11): 1397

54 Huang T, Liu Z L, Wu D C *et al. Journal of Materials Research and Technology*[J], 2021, 15: 226

55 Lei L, Cui Z Y, Pan H *et al. Corrosion Science*[J], 2022, 195: 109975

56 International Organization for Standardization. *Biological Evaluation of Medical Devices—Part 5: Test for in Vitro Cytotoxicity*, ISO 10993–5[S], 1999

57 Li X M, Shi Z Z, Zhang J Y *et al. Acta Biomaterialia*[J], 2025, 193: 584

Sr对Zn-Sn基可降解生物医学合金微观结构与性能的影响

彭浩东[1]，李　卓[2,3]，孙牧群[1]，陈英英[2,3]，赵琳琳[1]，张　欣[1]

(1. 天津理工大学 材料科学与工程学院，天津 300384)

(2. 天津中医药大学第一附属医院，天津 300193)

(3. 中医国家临床医学研究中心，天津 300193)

摘　要：研究了可生物降解Zn-1.5Sn-*x*Sr合金（*x*=0、0.3、0.5， wt%）的微观结构、力学性能、腐蚀行为及细胞毒性。结果表明，Sr元素的引入形成了微量$SrZn_{13}$相，提高了Zn-1.5Sn-*x*Sr合金的屈服强度和弹性模量。通过透射电子显微镜衍射斑点标定，证明了$SrZn_{13}$相的存在。电化学测试证实了Zn-1.5Sn-*x*Sr合金表面生成钝化膜，且Zn-1.5Sn-0.3Sr表现出更好的耐蚀性，进一步的浸泡测试与X射线光电子能谱分析揭示了腐蚀产物膜的元素组成及成分，主要由氧化物、氢氧化物以及微溶性碳酸盐和磷酸盐组成。在细胞毒性方面，Zn-1.5Sn-*x*Sr合金表现出优异的生物相容性。MTT实验显示细胞活力最高可达130%，这归因于材料降解过程中Sr^{2+}的释放，Sr^{2+}与Zn^{2+}共同促进了细胞增殖与分化。

关键词：生物医学合金；可降解合金；力学性能；生物相容性

作者简介：彭浩东，男，2000年生，硕士生，天津理工大学材料科学与工程学院，天津 300384，E-mail：18231781080@163.com；李 卓，女，1987年生，硕士，天津中医药大学第一附属医院，天津 300193，E-mail：lizhuo0310195@163.com